

1  
2  
3  
4  
5  
6  
7  
8

## Original Research Article

**2D-simulation of Nanopowder High-Speed  
Compaction****ABSTRACT**

The paper concerns the nanopowder high-speed,  $10^4 - 10^9 \text{ s}^{-1}$ , compaction processes modeling by a two-dimensional granular dynamics method. Nanoparticles interaction, in addition to known contact laws, included dispersive attraction, formation of a strong interparticle bonding (powder agglomeration) as well as the forces caused by viscous stresses in the contact region. For different densification rates, the “pressure vs. density” curves (densification curves) were calculated. Relaxation of the stresses after the compression stage was analyzed as well. The densification curves analysis allowed us to suggest the dependence of compaction pressure as a function of strain rate. It was found that in contrast to the plastic flow of metals, where the yield strength is proportional to the logarithm of the strain rate, the power-law dependence of applied pressure on the strain rate as  $p \propto \dot{\gamma}^{1/4}$  was established for the modeled nanosized powders.

9  
10  
11  
12  
13  
14  
15  
16  
17  
18  
19  
20  
21  
22  
23  
24  
25  
26  
27  
28  
29  
30  
31  
32  
33  
34  
35  
36  
37  
38  
39  
40  
41

*Keywords: nanopowder; granular dynamics method; discrete element method; high-speed compaction.*

**1. INTRODUCTION**

The nanopowder cold compaction is a very important stage of novel nanostructured materials production by the powder metallurgy [1, 2]. As known, nanopowders in contrast to coarse-grained materials are very hard to densify due to the strong interparticle “friction”, which is caused by the intense dispersion attraction, and agglomeration of particles [2, 3]. To achieve a proper compact density for sintering the high quality, defect-free ceramic article, applying the high pressure of about several gigapascals is required. Such high pressures can even exceed the durability of pressing tools [2 – 4]. Thus, the theoretical description of powder body and reliable forecasting the compaction processes take on high topicality.

The present paper is devoted to development of theoretical description of oxide nanosized powders cold compaction processes in the frameworks of the granular dynamics method [5, 6]. This method is of interest due to the oxide nanoparticles, for example, produced by the method of wires electric explosion [7] or target laser evaporation [8], usually have high strength properties and a spherical form. Therefore, such powders are the most convenient object for simulations. Nowadays the granular dynamics method is extensively used for description of compaction processes of different micro- and nanopowders [5, 6, 9, 10]. However at that quasistatic compaction processes are investigated. After every step of model cell deformation the new equilibrium locations of particles are determined during a large number of equilibration steps [5, 6].

In view of necessity to achieve extremely large compaction pressures the magnetic pulsed methods [2, 4] attract a great attention at present time. These methods allow increasing the pressure into compacts owing to the inertial effects. The relative rate of compact densification is of  $10^4 - 10^5 \text{ s}^{-1}$ . It is known that dynamical yield strength is not equal to static one, as a rule. For example, the yield strength of metal at high-speed loading can exceed the static limit by several times [11 – 13]. Corresponding studies for nanopowders have not been conducted yet.

## 42 2. NUMERICAL EXPERIMENT DETAILS

43

44 We simulate the dynamical processes of uniform pressing, which are characterized with the relative  
 45 densification rate  $v = (1/\rho)(d\rho/dt)$ , where  $\rho$  is density and  $t$  is time, from value  $6.8 \times 10^8 \text{ s}^{-1}$  up to  
 46  $6.8 \times 10^4 \text{ s}^{-1}$ . To perform the qualitative analysis we restrict to 2D geometry. The model cell has a form  
 47 of square  $L_{\text{cell}} \times L_{\text{cell}}$ . The density is implied as a relative area of the model cell occupied by the  
 48 particles, i.e.  $\rho = (\pi/4)N_p d_g^2 / L_{\text{cell}}^2$ , where  $N_p = 1000$  is the number of particles in the cell,  $d_g$  is the  
 49 particle diameter. Periodic boundary conditions are used on all the sides of the cell. For initial packing  
 50 generation, the algorithm defined in [5] is used, which allows us to create isotropic and uniform  
 51 structures in a form of the connected 2D-periodic cluster. The initial density  $\rho_0$  is 0.5. The system  
 52 deformation is performed by simultaneous changes of cell sizes and proportional rescaling of particles  
 53 coordinates. This procedure corresponds to the instantaneous propagation of elastic perturbation  
 54 along the model cell. The relative displacements and rotations of particles are determined by the  
 55 usual equations

56

$$57 \quad m \frac{d^2 r}{dt^2} = f, \quad J \frac{d^2 \theta}{dt^2} = M, \quad (1)$$

58

59 where  $m = (\pi/6)\rho_m d_g^3$  is the particle mass,  $\rho_m$  is the density of the particle material,  $f$  and  $M$  are  
 60 the total force and torque caused by other particles,  $J = m d_g^2 / 10$  is inertia moment,  $\theta$  is the rotation  
 61 angle. The Verlet algorithm [14] is applied for the numerical solve of the equation (1).

62

63 The stress tensor  $\sigma_{ij}$  averaged over the model cell is calculated by the known expression [5, 9, 10]

64

$$65 \quad \sigma_{ij} = \frac{-1}{d_g L_{\text{cell}}^2} \sum_{k < l} f_i^{(kl)} r_j^{(kl)}, \quad (2)$$

66

67 where the summation is performed over all pairs of interacting particles  $(k, l)$ ;  $f^{(k,l)}$  is the total force  
 68 affecting the particle  $k$  from the particle  $l$ ;  $r^{(k,l)}$  is the vector connecting the centers of the particles. The  
 69 particle interactions described in detail elsewhere [5, 6] include the elastic repulsion (modified Hertz  
 70 law), the "friction" forces (Cattaneo – Mindlin law), the dispersive attraction force (Hamaker's formula),  
 71 and the contact elasticity of flexure because of strong interparticle bonding. Alumina is implied as the  
 72 particle material for which, in particular, the Young modulus  $E$  is 382 GPa and the Poisson ratio  $\nu$  is  
 73 0.25. Other parameters of interaction laws correspond to the system of II type in [5, 6], which imitates  
 74 strongly agglomerating nanopowders [15] with particle diameter  $d_g = 10$  nm. The exception as  
 75 compared to the 3D simulations is only the larger value of friction coefficient  $\mu = 0.5$  used in the  
 76 present study.

77

78 The high value of speed of modeled processes requires taking into account the viscous stresses in the  
 79 vicinity of the contact area of particles. Using the similarity of Hooke's elastic law and the Navier –  
 80 Stokes equations the authors of [16] obtained the rigorous solution of the problem on contact  
 81 interaction of viscoelastic spheres. In general case the influence of the viscous stresses has a form  
 82 [16, 17]

83

$$84 \quad f_{\text{visc}} = A \frac{df_e}{d\zeta} \frac{d\zeta}{dt}, \quad (3)$$

85

86 where  $f_{\text{visc}}$  is the total force of the viscous stresses,  $f_e$  is the elastic force,  $\zeta$  is the variable, which  
 87 describes the body deformation, and the coefficient  $A$  neglecting the bulk viscosity is described as:

88

$$89 \quad A = \frac{\eta(1-\nu^2)(1-2\nu)}{3E\nu^2} .$$

90

91 The shear viscosity coefficient  $\eta$  is estimated by the known data on ultrasound damping into alumina  
 92 [18]. The coefficient of damping into the isotropic medium  $\gamma_t = \eta\omega^2 / (2\rho_m c_t^3)$  [19], where  $\omega$  and  $c_t$   
 93 are the frequency and speed of sound. Using the value  $\gamma_t \cong 230$  dB/m at the frequency of  $\omega / 2\pi = 1.0$  GHz  
 94 [20] the shear viscosity coefficient  $\eta$  for alumina of 0.001 Pa·s was obtained.

95

96 Starting from the equation (3) it is not difficult to write all expressions which describe the interactions of  
 97 viscoelastic spherical particles. For example, for linearized tangential force of “friction” we have  
 98

99

$$\frac{f_t}{E} = c_m a \delta + A c_m a \frac{d\delta}{dt}, \quad c_m = \frac{4}{(2-\nu)(1+\nu)},$$

100

101 where  $\delta$  is the relative tangential displacement of contacting particles,  $a = \sqrt{hd_g} / 2$  is the contact spot  
 102 radius,  $h = d_g - r$  is the depth of particle overlapping.

103

104 The characteristic time  $T = ((\pi\rho_m d_g^2) / (6E))^{1/2}$ , which transforms the equations (1) to dimensionless  
 105 form, is equal to 0.74 ps for our systems. The reduced time step of the numerical solving the equations  
 106 (1) is  $h_t = h_{t,d} / T = 0.04$ . The relative decreases of model cell sizes  $\Delta L_{\text{cell}} / L_{\text{cell}}$  corresponding to the time  
 107 step are equal to values  $10^{-5}$ ,  $10^{-6}$ ,  $10^{-7}$ ,  $10^{-8}$ , or  $10^{-9}$ . These values result in strain rates (in  $\text{s}^{-1}$ ):  
 108  $v_1 = 6.8 \times 10^8$ ,  $v_2 = 6.8 \times 10^7$ ,  $v_3 = 6.8 \times 10^6$ ,  $v_4 = 6.8 \times 10^5$ , and  $v_5 = 6.8 \times 10^4$ .

109

110

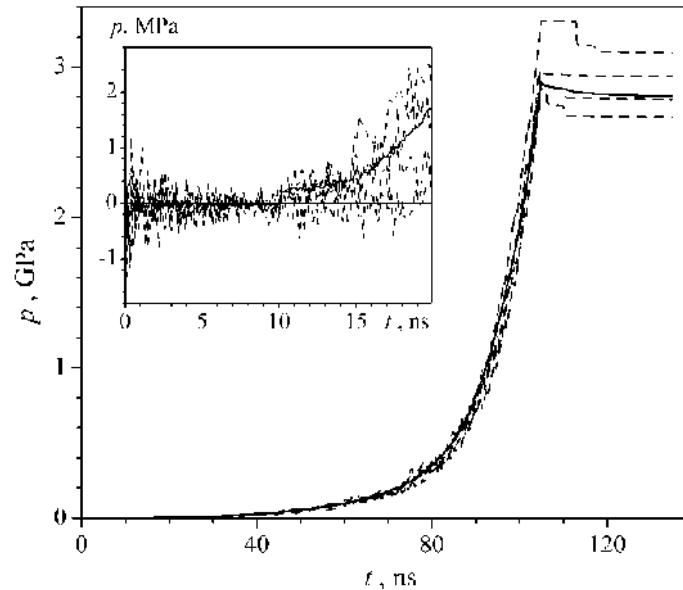
### 111 3. RESULTS AND DISCUSSION

112

113 Figure 1 presents the time-dependent hydrostatic pressure  $p = \text{Sp}(\sigma_{ij}) / 2$  averaged over 80 calculations  
 114 and typical calculation curves for the compression rate  $v_3$ . Averaging the other rates has been  
 115 performed over 100 ( $v_1$ ,  $v_2$ ) and 10 ( $v_4$ ) independent calculations. For the rate  $v_5$  the only one  
 116 calculation has been carried out.

117

118



119

120

121 **Fig. 1. The time dependence of pressure for the densification rate  $v_3 = 6.8 \times 10^6 \text{ s}^{-1}$ . Dashed**  
 122 **lines are examples of calculation curves, solid line is the average over 80 independent**  
 123 **calculations. Insert shows the period of the preliminary relaxation (10 ns) and the beginning of**  
 124 **the compression.**

125  
126

127 It is helpful to note that the initial structures are being generated by the algorithm [5], which places the  
128 neighboring particles at equilibrium distances when attraction compensates repulsion, requires however  
129 a preliminary relaxation step. It is needed since the dispersion forces between further particles are not  
130 taken into account in the algorithm that results in slight fluctuations of particles in the initial structure. In  
131 order to extinguish the fluctuations, initially generated structure relaxes for 10 ns (see the inset in Fig. 1).  
132

133 Compression of the model cell was performed up to the density  $\rho = 0.95$  where the pressure arrives at  
134 about 3 GPa. After that the system was relaxed during 30 ns. A considerable reduction of stresses is  
135 observed at this relaxation stage. This reduction for the hydrostatic pressure is well approximated by an  
136 expression  
137

$$p(t) = p_0 + p_1 \exp(-t / \tau_1) + p_2 \exp(-t / \tau_2), \quad (4)$$

139

140 Coefficients of the approximation (4) for the simulated strain rates are presented in Table 1. Post-  
141 compression relaxation proceeds in two stages: "rapid" with a characteristic time of about tenths of  
142 nanoseconds, and "slow", which lasts from several up to tens of nanoseconds. Change of hydrostatic  
143 pressure during relaxation decreases from 441 MPa (it is about 17% of the compaction pressure) at the  
144 densification rate  $v_1$  almost to zero at the rate  $v_5$ . So, the compaction of the model system at the  
145 densification rate of the order of  $10^4 \text{ s}^{-1}$  can be considered as a nearly quasistatic process.  
146

146

147

148

**Table 1. The coefficients of approximations (4)**

	$p_0$ , MPa	$p_1$ , MPa	$\tau_1$ , ns	$p_2$ , MPa	$\tau_2$ , ns
$v_1$	2603.9	441.1	0.0719	35.3	4.9304
$v_2$	2810.3	109.7	0.1977	72.0	4.3350
$v_3$	2803.2	13.3	0.4486	84.1	9.2157
$v_4$	2835.1	49.8	0.1515	29.0	10.0
$v_5$	2868.6	0.0	—	1.31	30.0

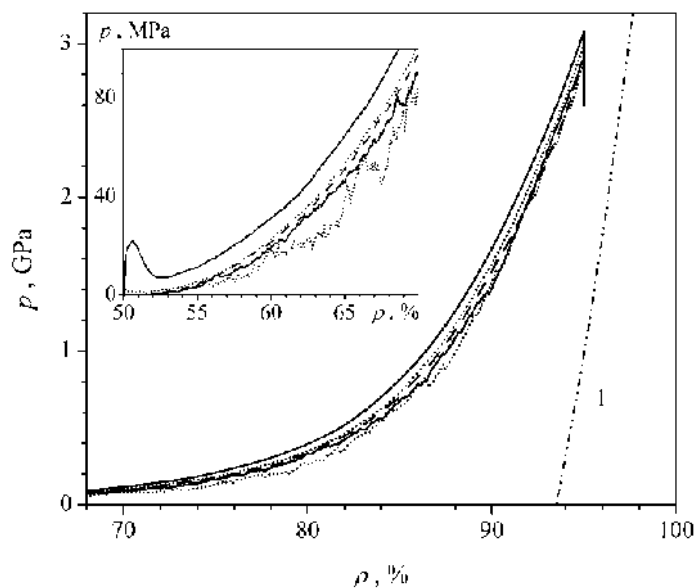
149

150

151 Fig. 2 presents the compaction curves corresponding to the different densification rates. It is interesting  
152 that the  $p(\rho)$  curve for  $v_1$  rate has a local maximum at the beginning, which is very similar to the yield  
153 drop at stress-strain curves of metals [21]. This maximum has a dynamical nature and is caused by the  
154 retardation of relaxation processes from the powder compression. According to the simulation results,  
155 an increase in pressure up to the local maximum takes about 0.02 ns. This time is significantly less than  
156 the time of the "rapid" relaxation, which is about 0.07 ns (see Table 1) at the rate  $v_1$ . At slower  
157 densification rates this maximum disappears.  
158

158

159



160  
161  
162  
163  
164  
165  
166  
167

**Fig. 2. Densification curves in “density – pressure” coordinates for strain rates  $v_1$  (left solid line),  $v_2$  (left dotted line),  $v_3$  (dashed line),  $v_4$  (right solid line), and  $v_5$  (right dotted line). Line 1 is the asymptotic curve according to the eqs. (5) – (8). Insert shows the low pressure region in the expanded scale.**

168 As one can see on the Fig. 2, all the densification curves can be adequately approximated in the limit of  
169 large densities and pressures. To obtain the asymptote we use the interrelation of regular packing  
170 density of the disks on the plane with mean coordination number  $k_{av}$  (the number of particle contacts) in  
171 the form

172

173

$$\rho_{reg} = \frac{\pi / k_{av}}{\tan(\pi / k_{av})}. \quad (5)$$

174

175 At high pressures we can expect strong friction forces between particles. It should result to that the  
176 uniform compression of the system proceeds without relative displacement of particles. In such a case  
177 the density increases in 2D geometry as

178

179

$$\rho(h) = \frac{\rho_{reg}}{(1 - h / d_g)^2}. \quad (6)$$

180

181 For the hydrostatic pressure from Eq. (2) we have [9, 10]

182

183

$$p = \frac{\rho k_{av}}{\pi d_g^3} \langle f_n(h)(d_g - h) \rangle, \quad (7)$$

184

185 where  $f_n$  is the normal part of the contact force without taking into account the viscous stresses, and  
186 angle brackets mean the average over the all pairs of interacting particles. Replacing  $\langle \dots \rangle$  in Eq. (7)  
187 with the corresponding interaction laws we get the dependence of  $p(\rho)$ , which is implicitly determined  
188 by the equations (5) – (7) where the mean coordination number  $k_{av}$  is a parameter. According to the  
189 analysis of simulation results, the interrelation of coordination number  $k_{av}$  with density for all the strain  
190 rates is well described by the expression

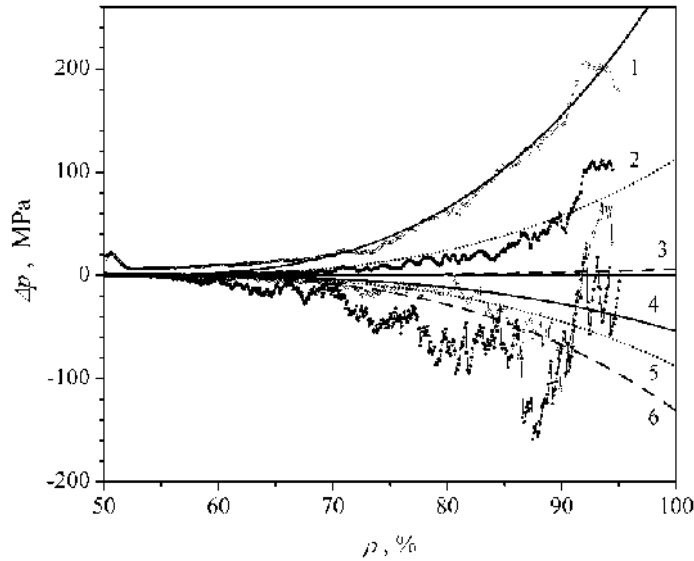
191

192

$$k_{av} = 2.3 + 3.0\rho^2. \quad (8)$$

193  
194  
195  
196  
197  
198

The asymptote relationship  $p(\rho)$  determined by the equations (5) – (8) is shown in Fig. 2 (curve 1). It can be seen that the densification curves  $p(\rho)$  reach the asymptote in the high pressure limit. At the pressure of 3 GPa the error in the density according to the asymptote is less than 3%.



199  
200  
201  
202  
203  
204  
205  
206  
207  
208  
209  
210

**Fig. 3. The differences of compaction pressures from the pressure corresponding to the rate  $v_3$  as a function of density. Symbols are the simulation results for rates  $v_1, v_2, v_4,$  and  $v_5$  (from the top); smooth lines are the dependences of Eq. (9) for the densification rates  $v_1 - v_5$  and for the quasistatic conditions (the line 6).**

211  
212  
213  
214  
215  
216  
217  
218  
219  
220  
221  
222

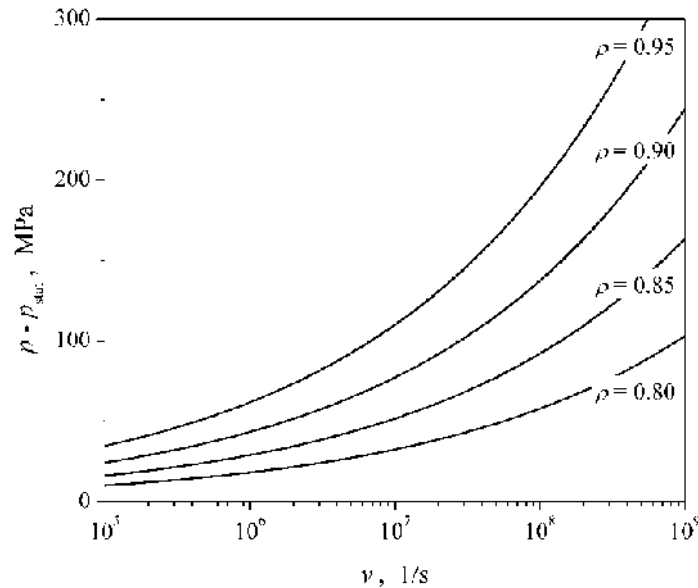
To analyze the dependencies in Fig. 2, the densification curve  $p(\rho)$  corresponding to the rate  $v_3$  has been used as a reference one. Fig. 3 shows the differences between the other densification curves and the reference one. These differences are well approximated by the expression:

$$p(\rho, v) = p_3(\rho) + p_v(v)(\rho - \rho_0)^\gamma.$$

The analysis performed reveals that the index  $\gamma \cong 3$ , and the strain-rate-dependent coefficient  $p_v$  is well described by the expression  $p_v = p_{v0} + k_v v^{1/4}$ . As a result, taking the quasistatic conditions ( $v \rightarrow 0$ , the line 6 in Fig. 3) as a reference line we have obtained

$$p(\rho, v) = p_{\text{stat}}(\rho) + k_v v^{1/4} (\rho - \rho_0)^3. \quad (9)$$

where  $k_v = 21.5 \text{ MPa s}^{1/4}$ . Fig. 4 demonstrates the influence of compression rate on the acting pressure, which is determined by the equation (9).



223  
224  
225 **Fig. 4. Difference between dynamical and static compaction pressure at preset values of**  
226 **compact density as a function of strain rate.**  
227

228  
229 For example, it can be seen from Fig. 4 that achievement of the density  $\rho = 0.95$  with the strain rate  
230  $v = 10^8 \text{ s}^{-1}$  requires the pressure, which is larger than that at quasistatic process by 200 MPa.  
231

#### 232 233 4. CONCLUSION

234  
235 For the first time, the influence of the compression rate on the compactibility of oxide nanopowders has  
236 been studied by a two-dimensional granular dynamics method. Processes of stress relaxation after the  
237 stage of high-speed compression with the strain rates of  $10^4 - 10^9 \text{ s}^{-1}$  up to the relative density  $\rho = 0.95$   
238 have been analyzed. In particular, it has been found that the time of the stress relaxation is about 10 ns  
239 when the strain rate decreases down to  $10^6 \text{ s}^{-1}$ . At this case the decrease of the mean pressure at the  
240 relaxation stage does not exceed 100 MPa which is significantly smaller than the compaction pressure  
241 (about 3 GPa). The explicit dependence of the compaction pressure, which is connected with the yield  
242 strength within phenomenology of powder body [1], on the strain rate has been established. It has been  
243 found that in 2D geometry, nanosized powders demonstrate the power-law dependence of pressure on  
244 strain rate as  $p \propto v^{1/4}$ , in contrast to plastic flow of metals, where the yield strength is proportional to the  
245 logarithm of the strain rate [12].  
246

#### 247 248 REFERENCES

- 249  
250 1. Shtern MB, Serdyuk GG, Maksimenko LA, Truhan YV, Shulyakov YM. Phenomenological  
251 Theories of Powder Pressing. Kiev: Naukova Dumka; 1982. Russian.  
252 2. Boltachev GS, Nagayev KA, Pararin SN, Spirin AV, Volkov NB. Magnetic Pulsed Compaction of  
253 Nanosized Powders. NY: Nova Science Publishers, Inc.; 2010.  
254 3. Filonenko VP, Khvostantsev LG, Bagramov RK, Trusov LI, Novikov VI. Compacting tungsten  
255 powders with varying particle size using hydrostatic pressure up to 5 GPa. Powder Metallurgy  
256 and Metal Ceramics. 1992;31(4):296-299.  
257 4. Olevsky EA, Bokov AA, Boltachev GS, Volkov NB, Zayats SV, Ilyina AM, et al. Modeling and  
258 optimization of uniaxial magnetic pulse compaction of nanopowders. Acta Mechanica.  
259 2013;224(12):3177-3195.  
260 5. Boltachev GS, Lukyashin KE, Shitov VA, Volkov NB. Three-dimensional simulations of  
261 nanopowder compaction processes by granular dynamics method. Physical Review E.

- 262 2013;88(1):012209.
- 263 6. Boltachev GS, Volkov NB, Kochurin EA, Maximenko AL, Shtern MB, Kirkova EG. Simulation of  
264 the macromechanical behavior of oxide nanopowders during compaction processes. *Granular*  
265 *Matter*. 2015;17(3):345-358.
- 266 7. Kotov YA. Electric Explosion of Wires as a Method for Preparation of Nanopowders. *Journal of*  
267 *nanoparticle research*. 2003;5(5-6):539-550.
- 268 8. Kaygorodov AS, Ivanov VV, Khrustov VR, Kotov YA, Medvedev AI, Osipov VV, et al. Fabrication  
269 of Nd:Y2O3 transparent ceramics by pulsed compaction and sintering of weakly agglomerated  
270 nanopowders. *Journal of the European Ceramic Society*. 2007;27(2-3):1165-1169.
- 271 9. Agnolin I, Roux JN. Internal states of model isotropic granular packings. I. Assembling process,  
272 geometry, and contact networks. *Physical Review E*. 2007;76:061302.
- 273 10. Gilibert V, Roux JN, Castellanos A. Computer simulation of model cohesive powders: Plastic  
274 consolidation, structural changes, and elasticity under isotropic loads. *Physical Review E*.  
275 2008;78:031305.
- 276 11. Regel' VR, Slutsker AI, Tomashevskii ÉE. The kinetic nature of the strength of solids. *Physics-*  
277 *Uspekhi*. 1972;15:45-65.
- 278 12. Vasin RA, Lensky VS, Lensky EV. Problems of the dynamics of elastic-plastic continuum, 7.  
279 Moscow: Mir; 1975. Russian.
- 280 13. Belan VG, Durmanov ST, Ivanov IA, Levashov VF, Podkovyrov VL. Energy loss by plastic  
281 deformation in radial compression of a cylindrical shell. *Journal of Applied Mechanics and*  
282 *Technical Physics*. 1983;24(2):236-242.
- 283 14. Allen MP, Tildesley DJ. *Computer Simulation of Liquids*. Oxford: University Press; 2003.
- 284 15. Boltachev GS, Volkov NB, Kaygorodov AS, Loznukho VP. The Peculiarities of Uniaxial  
285 Quasistatic Compaction of Oxide Nanopowders. *Nanotechnologies in Russia*. 2011;6(9-10):639-  
286 646.
- 287 16. Brilliantov NV, Spahn F, Hertzsch JM, Pöschel T. Model for collisions in granular gases. *Physical*  
288 *Review E*. 1996;53(5):5382-5392.
- 289 17. Brilliantov NV, Pöschel T. *Kinetic Theory of Granular Gases*. Oxford: University Press; 2004.
- 290 18. Boltachev GS, Spirin AV, Chingina EA. Simulation of high-speed compaction processes of  
291 nanopowders by 2D granular dynamics method. XVII All-Russian school-seminar on condensed  
292 matter problems (SPFKS-17), 185. Ekaterinburg: IMP UB RAS; 2016. Russian.
- 293 19. Landau LD, Lifshitz EM. *Theory of Elasticity*. Oxford: Pergamon Press; 1993.
- 294 20. Grigoriev IS, Meilikhov EZ, editors. *Physical Quantities: Handbook*. Moscow: Energoatomizdat;  
295 1991. Russian.
- 296 21. Petrov YV, Borodin EN. Relaxation mechanism of plastic deformation and its justification using  
297 the example of the sharp yield point phenomenon in whiskers. *Physics of the Solid State*.  
298 2015;57(2):353-359.